THE JOURNAL OF PHYSICAL CHEMISTRY C
A JOURNAL OF THE AMERICAN CHEMICAL SOCIETY

pubs.acs.org/JPCC

Article

Heavy versus Light Lanthanide Selectivity for Graphene Oxide Films Is Concentration-Dependent

Published as part of The Journal of Physical Chemistry virtual special issue "Early-Career and Emerging Researchers in Physical Chemistry Volume 2".

Amanda J. Carr, Seung Eun Lee, and Ahmet Uysal*

Cite This: *J. Phys. Chem. C* 2023, 127, 14363−14373

Read Online

ACCESS | Metrics & More | Article Recommendations | Supporting Information

ABSTRACT: Rare earths are important materials in various technologies such as catalysis and optoelectronics. Graphene oxide (GO) is a promising material for separation applications, including the isolation of lanthanides from complex mixtures. Previous works using fatty acid monolayers have demonstrated preferential heavy versus light lanthanide adsorption, which has been attributed to differences in lanthanide ion size. In this work, we used interfacial X-ray fluorescence measurements to reveal that GO thin films at the air/water interface have no lanthanide selectivity for dilute subphases. However, at high subphase concentrations, ∼8 times more Lu is adsorbed than La. By comparing the GO results with an ideal monolayer with a carboxylic acid headgroup, arachidic acid (AA), we demonstrate that the number of Lu ions adsorbed to GO is significantly higher than the number expected to compensate for the surface charge. Vibrational sum frequency generation (SFG) spectroscopy results on both GO thin films and AA monolayers reveal a red-shifted SFG signal in the OH region, which we attribute to partial dehydration of the adsorbed ions and carboxylic acid headgroups. Liquid surface X-ray reflectivity data show that the GO thin film structure does not significantly change between the very dilute and concentrated subphases. We speculate that the functional groups of both GO and AA facilitate cation dehydration, which is essential for ion adsorption. Heavy lanthanide Lu has stronger ion−ion correlations that can overcome the electrostatic repulsion between cations at higher concentrations compared to light lanthanide La, meaning GO and AA can exhibit apparent overcharge with Lu. Lastly, the layered structure of the GO films and reactive chemical nature of GO itself can accommodate ion adsorption.

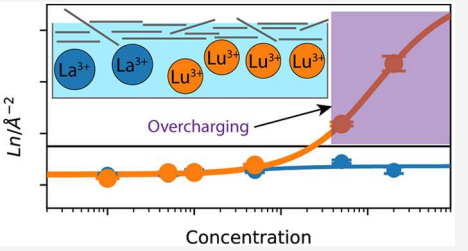

INTRODUCTION

Isolating lanthanides from complex mixtures is critical for a range of applications including catalysis and petroleum refining, medical imaging, permanent magnet fabrication, optoelectronics, and green technology development among others.[1−4] Graphene oxide (GO) is a promising[5] two-dimensional amphiphile due to its sp^2 hybridized carbon backbone decorated with oxygen functional groups including carboxylic acids, epoxies, and hydroxyls.[6] The exact chemical and physical structures vary depending on the synthesis,[7] but GO usually exists as flakes with hydrophobic basal planes and hydrophilic edges.[8,9] Bulk experimental and computational works have investigated rare earth,[10−13] actinide,[11,14−18] and other metal separations[19−22] using GO, typically through bulk adsorption of the metal ions onto the GO flakes or filtration via GO membranes consisting of stacked GO flakes. Arguably, the nanoscale interactions governing the success of these separations occur in the small, interfacial region formed between the GO flakes and liquid. Recent works have probed this interface by creating GO thin films directly on aqueous subphases,[23−28] and a recent work by our group connected interfacial interactions with GO to rare earth metal separation performance using GO membranes.[29]

Interestingly, the extraction efficiency of metals across the lanthanide series varies even though nearly all ions are trivalent in typical aqueous conditions.[1,2,30−32] These differences have been attributed to lanthanide contraction,[33,34] where the atomic radius of the metal decreases as the atomic number increases. This small but important variation in the ion size strongly affects hydration structures,[35] coordination chemistry,[36] and solvation enthalpies.[37] Indeed, studies have probed changes in the hydration structure of the lanthanides across the series.[38] X-ray scattering and molecular dynamics simulations[35] have shown a gradual transition from ∼9 to ∼8 waters in the first coordination shell from La^{3+} to Lu^{3+}. The hydration structure of ions at the air/water interface is directly relevant to

Received: February 27, 2023
Revised: June 7, 2023
Published: July 14, 2023

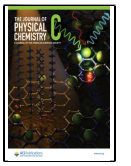

separation efforts, as ions may undergo partial or total dehydration during adsorption.[32,39,40] Recently, our group studied Nd adsorption to arachidic acid (AA) films using vibrational sum frequency generation spectroscopy (SFG) and observed a red-shifted signal within the water region, which was attributed to the partial dehydration of adsorbed Nd ions.[41] SFG is an inherently surface-specific technique that is well suited to understand local water structures near the air/water interface as the signal is only generated when centrosymmetry is broken (Figure 1).[39,40,42−44]

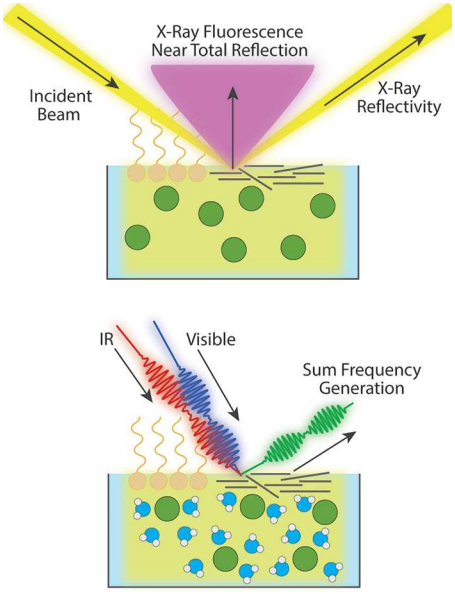

Figure 1. Experimental cartoon showing AA (tan) monolayers and GO (gray) thin films at the air/water interface. X-ray fluorescence (top), XR (top), and SFG spectroscopy (bottom) are interface-specific techniques that detail the adsorbed ion density, monolayer or film structure, and water organization, respectively.

In this work, we consider both light lanthanide La and heavy lanthanide Lu adsorption to a GO thin film and an ideal AA monolayer at the air/water interface to understand the effects of ion size on adsorption and local water structure. AA serves as a model monolayer composed of well-organized carboxylic acid headgroups each with a hydrocarbon tail. This comparison allows us to quantify the density of carboxylic acid groups on GO and to resolve the ambiguities due to the interference effects in the SFG signal.[26] Surface X-ray fluorescence near total reflection (XFNTR) measurements on GO and AA monolayers (Figure 1) allow quantitative determination of adsorbed La and Lu ions[45] and reveal that GO thin films adsorb 8.3× more Lu versus La when placed on a high-concentration subphase. By comparing this adsorbed ion density to that of AA and examining the thin film structure with liquid surface X-ray reflectivity (XR) (Figure 1), we show that the GO films exhibit apparent overcharging for Lu, i.e., significantly more Lu ions adsorb than the amount expected to compensate the surface charge of GO. However, La ions do not show overcharging. Strikingly, for dilute subphases, La and Lu adsorption to GO thin films is nearly identical with no noticeable selectivity. Additionally, the XFNTR measurements explicitly show apparent overcharging of the AA monolayer when Lu is present, while La adsorption follows the expected charge compensation. This is the first time, to the best of our knowledge, that apparent overcharging on AA with only a heavy lanthanide has been demonstrated. These results are coupled with SFG measurements that show the emergence of a signal attributed to partially dehydrated adsorbed ions that is present for both GO thin films and AA monolayers. We posit that the functional groups of GO and AA facilitate partial ion dehydration and allow adsorption, as evidenced by our SFG results. Lastly, we speculate that GO thin films can accommodate more adsorbed ions because of their complex layered structure and the reactive chemistry of GO.

EXPERIMENTAL SECTION

Materials and Sample Preparation. All samples were prepared using ultrapure water (resistivity = 18.2 MΩ, Millipore, Synergy Water Purification system). We considered two surfactants: AA and GO. 1 mM AA samples (Sigma-Aldrich) were prepared using 3:1 chloroform/methanol (v/v, Sigma-Aldrich) and were stored at 0 °C. GO samples were made by sonicating a commercially available stock solution of 10 mg/mL GO (purchased from Standard Graphene, South Korea) for 5 min and then diluting it to 1 mg/mL with water. Samples were diluted again 1:5 with anhydrous methanol (Sigma-Aldrich), sonicated for 1 h, and lastly filtered through a 1.2 μm syringe filter. This GO preparation method allows smooth, reproducible thin films to be formed at the interface, as investigated in another work.[24] Metal solution samples were prepared using $LaCl_3{\cdot}7H_2O$ (99.999% trace metal basis) and $LuCl_3{\cdot}6H_2O$ (≥99.99% trace metal basis) (Sigma-Aldrich). The pH of the subphases was not adjusted and was approximately 6, meaning nearly all carboxylic acid groups of AA and GO were fully deprotonated.[29]

Synchrotron X-ray Measurements. Liquid surface XR and XFNTR measurements were completed at Sector 15ID-C, ChemMatCARS, at the Advanced Photon Source at Argonne National Laboratory. The incident X-ray beam at 10 keV was focused using various optics and the final size is 2 mm horizontal by 40 μm vertical set using slits.

Samples were prepared in a polytetrafluoroethylene-coated Langmuir trough, with a single barrier and a pressure sensor (Nima) equipped with a clean Wilhelmy plate made of chromatography paper, placed inside a containment box. A custom glass slab cleaned using Nochromix was placed in the trough to reduce the trough volume to 200 mL. The trough was thoroughly cleaned before each sample by wiping it with chloroform and alcohol and then rinsing it two to three times with clean water. 200 mL of the liquid subphase was placed in the trough, and the surface was cleaned to eliminate contamination. After cleaning, the surfactant, either AA or GO, was slowly spread on top of the subphase using an appropriately sized glass syringe (Hamilton). For these measurements, we spread 150 μL of AA and 200 μL of GO. The barrier was slowly closed until the target surface pressure was obtained, 10 mN/m for AA and 20 mN/m for GO. A surface pressure of 20 mN/m was chosen for GO because it placed enough GO at the interface to create a continuous, reproducible film. Lower surface pressures likely have spaces in between the GO sheets, which can complicate analysis. The final area depends on the surfactant. The containment chamber was purged with He gas, which reduced X-ray damage to the sample during the measurement and minimizes unwanted background scattering in air. He was bubbled through water prior to purging to keep the humidity consistent.

https://doi.org/10.1021/acs.jpcc.3c01350
J. Phys. Chem. C 2023, 127, 14363−14373

Liquid Surface XR Measurements and Fitting. After aligning the liquid sample height, reflectivity data was collected by measuring the specular reflection of the incident X-ray beam off the liquid surface as a function of the momentum transfer $Q_Z = (4\pi/\lambda) \sin(2\alpha/2)$, where λ is the wavelength of the incident beam, 1.24 Å, and α is the angle between the incident beam and sample surface. The reflections were measured on a Pilatus 200K detector. The sample was horizontally shifted at different points during the scan to reduce beam damage effects, and a few data points were re-collected to check reproducibility. Both AA monolayers and GO thin films showed reproducible XR signals across the horizontal sample area, meaning the samples were homogeneous.

Obtained XR data for GO are modeled using three slabs each with its own thickness and electron density, and a global roughness parameter. The roughness of these non-sharp, layered interfaces was dominated by surface capillary waves; hence, the roughness of each slab was set to be equal through the global roughness parameter. The slab parameters were determined using the recursive Parratt formalism via least-squares fitting to the following merit function (eq 1)

$$\chi^2 = \sum_{i=1}^{N} \frac{(R_{\mathrm{calc}_i} - R_{\mathrm{exp}_i})^2}{\gamma_i^2} \tag{1}$$

where R_{calc} is the calculated reflectivity, R_{exp} is the experimentally measured reflectivity, and γ is the uncertainty for each slab i. Reflectivity data were fit using StochFit,[46] and fit parameters are provided in the Supporting Information (Table S1).

X-ray Fluorescence Near Total Reflection Measurements and Fitting. Fluorescence intensities were collected on a Vortex-60EX multi-cathode energy-dispersive detector positioned 10.4 mm perpendicular to the liquid surface sample. Detector calibration data were collected by measuring a 20 mM metal subphase sample without a surfactant. Measured fluorescence data were collected on prepared samples with a surfactant, either AA or GO. All fluorescence energies are recorded simultaneously over Q_Z, and the target subphase ion emission energy was extracted after the measurement by fitting the emission energy to a Gaussian peak with a polynomial background. Consequently, we could assess subphase metal ion contamination, which was insignificant in our measurements. This process was repeated for each measured value of Q_Z.

XFNTR data were fit by calculating the penetration depth and area of the incident X-ray based on the beam parameters and fitting the surface density of fluorescent ions necessary to generate a signal from that calculated area. As Q_Z varies, only the penetration depth of the beam changes because the beam footprint on the liquid sample is always larger than the area of the detector. We measured Q_Z around the critical angle $Q_C = 4\sqrt{\pi r_{e^-} \Delta\rho}$, where r_{e^-} is the classical radius of an electron and $\Delta\rho$ is the electron density contrast between the liquid subphase and air. For these samples, $Q_C \sim 0.022$ Å^{-1}. At $Q_Z < Q_C$, the signal undergoes total external reflection and only the evanescent waves penetrate the first few nanometers of the liquid, meaning the measured fluorescence signal is limited to ions at the interface. At $Q_Z > Q_C$, a fluorescence signal is generated from the bulk and interface.[45] Data were fitted using liquid surface software freely available from ChemMatCARS. All data and fits (Figures S2 and S3) and the fitted parameters (Table S1) are reported in the Supporting Information. For the GO samples, ions were placed at a fitted distance away from the liquid surface[29] to account for the partial submersion of the multilayered GO film, as characterized explicitly with liquid surface XR. We speculate that some GO may dissolve in the subphase and attract ions, although our XR analysis shows that more GO is contained at the air/water interface.

After fitting the XFNTR data to determine the surface density of adsorbed ions, data were plotted over concentrations of $LaCl_3$ and $LuCl_3$ for both AA and GO. Linear plots are provided in the Supporting Information (Figure S4). The concentration isotherms for La were fitted to a Langmuir adsorption model with one binding event (eq 2)

$$\theta = \theta_{\mathrm{Max}} \left(\frac{K_B C}{1 + K_B C} \right) \tag{2}$$

where θ is the absorbed ion coverage, θ_{Max} is the maximum adsorbed ion coverage, K_B is the adsorbed ion binding affinity, and C is the subphase concentration.[47] Concentration isotherms for Lu could not be described using a Langmuir adsorption model with one binding event and were instead fitted to a Langmuir adsorption model with two binding events (eq 3)

$$\theta = \theta_{\mathrm{Max},1} \left(\frac{K_{B,1} C}{1 + K_{B,1} C} \right) + \theta_{\mathrm{Max},2} \left(\frac{K_{B,2} C}{1 + K_{B,2} C} \right) \tag{3}$$

in which subscripts 1 and 2 refer to binding events 1 and 2, respectively.[48] Because determining the absolute values of K requires additional very low concentration data, these fits are only included as guides to the eye and for qualitative analysis.

Sum Frequency Generation Spectroscopy Measurements. SFG samples were prepared by slowly spreading a small amount of either AA or GO dropwise on an approximately 22 mL subphase in a polytetrafluoroethylene dish (inner diameter of 60 mm and a height of 20 mm) while monitoring the surface pressure with a sensor (Nima) equipped with clean chromatography paper. 25 μL of AA was added such that the surface pressure was 10 mN/m and 100 μL GO was added to give a surface pressure of 20 mN/m. All data were collected at room temperature under regular air.

SFG measurements were conducted using an EKSPLA system, which has been described in detail elsewhere.[39,43,49] In brief, an amplified Nd/YAG laser produces 20 ps pulses with 28 mJ power centered at 1064 nm at a rate of 50 Hz. This 1064 nm beam is split into two 532 nm beams. One is used as the visible-light source to measure the sample, and the other is used to generate a tunable IR signal using the original 1064 nm beam. These two signals are overlapped spatially and temporarily at the liquid surface to generate the SFG signal. The 532 nm beam was attenuated to 200 μJ, and the IR beam was attenuated to 100 μJ power during the measurements. The angles of incidence for the 531 nm and IR beams are 60 and 55° normal to the surface, respectively. The generated SFG signal was detected by a photomultiplier tube connected to a monochromator. Each spectrum was measured over the vibrational water range from 3000 to 3800 cm^{-1} using 4 cm^{-1} steps. Each datum point is an average of 300 laser shots. To avoid sample damage, the sample was rotated after every three frequency steps. This rotation also ensures that the samples are homogeneous and reproducible as data were measured and compared to ensure consistency. All presented

https://doi.org/10.1021/acs.jpcc.3c01350
J. Phys. Chem. C 2023, 127, 14363−14373

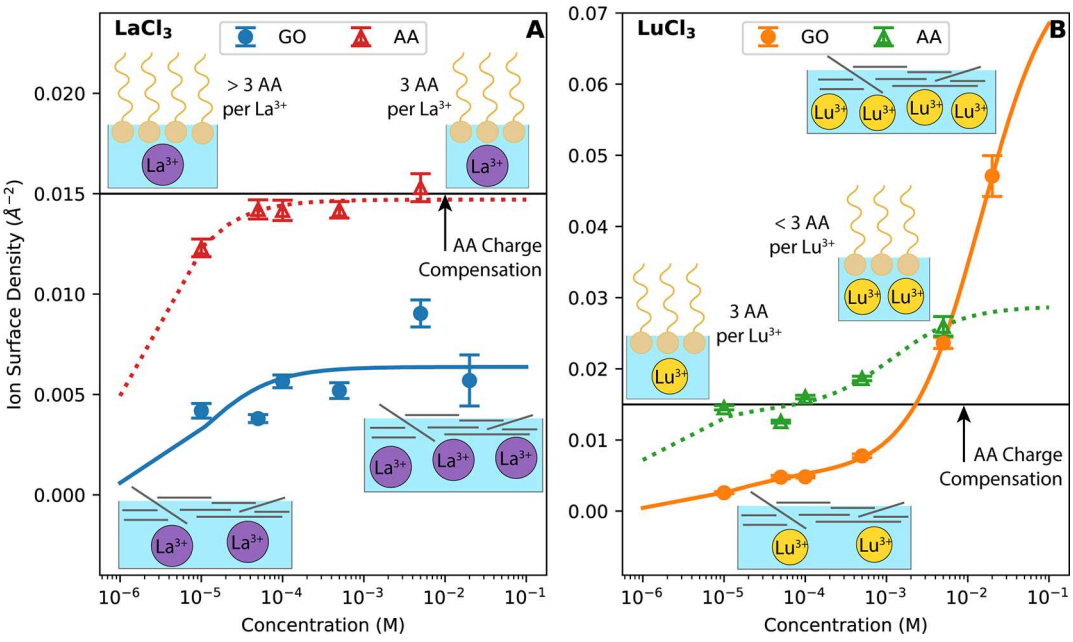

Figure 2. Adsorbed ion surface densities for $LaCl_3$ (A) and $LuCl_3$ (B) on GO thin films (circles) and AA monolayers (triangles) plotted over subphase concentration. Ion surface densities were calculated from fitted XFNTR data, and error bars are derived from those fits. Obtained ion surface densities qualitatively match Langmuir adsorption models with one binding event for $LaCl_3$ (eq 2) and two binding events to $LuCl_3$ (eq 3), which are included as guides to the eye. The trivalent ion surface density required for AA charge compensation is shown (solid black line). Cartoons are not to scale. Linear plots are provided in the Supporting Information. Note the *y*-scale changes between the two panels.

SFG data were normalized to a reference z-cut quartz (MTI Corporation). Data were collected by SSP polarization.

All collected SFG data (Supporting Information), I_{SFG}, are proportional to the effective $\chi^{(2)}$ signal, $\chi^{(2)}_{eff}$, and can be fitted to a series of n Lorentzian peaks using

$$I_{SFG} \propto \chi^{(2)}_{eff} \propto \left| \chi_{NR} + \sum_n \frac{A_n}{\omega_{IR} - \omega_n + i\Gamma_n} e^{i\phi_2} \right|^2 \quad (4)$$

where χ_{NR} is the non-resonant contribution, A_n is the peak amplitude, ω_{IR} is the IR frequency, ω_n is the resonant peak frequency, Γ_n is the dampening constant that determined peak width, and ϕ_2 is the phase between the resonant and non-resonant signals.[50] Data fitted over all concentrations via the sum of least-squares to eq 4 using three peaks centered around approximately 3100, 3200, and 3400 cm^{-1} to describe the emerging red-shifted signal, strongly hydrogen-bonded water, and weakly hydrogen-bonded water, respectively. The peak widths and frequencies, χ_{NR}, and ϕ_2 were global parameters and fitted across the concentration series, while the peak amplitudes were fitted individually for each concentration. All fits (Figures S5 and S6) and parameters (Tables S3 and S4) are provided in the Supporting Information.

Samples with charged surfaces can induce an additional SFG signal called the $\chi^{(3)}$ effect, defined as

$$I_{SFG} \propto \chi^{(2)}_{eff} \propto \left| \chi_{NR} + \sum_n \frac{A_n}{\omega_{IR} - \omega_n + i\Gamma_n} e^{i\phi_2} + \frac{\kappa}{\sqrt{\kappa^2 + \Delta k_Z^2}} e^{i\phi_3} \chi^{(3)} \Phi_0 \right|^2 \quad (5)$$

in which κ is the inverse Debye length, Δk_Z is the inverse SFG coherence length, ϕ_3 is the phase angle, $\chi^{(3)}$ is an explicit contribution, and Φ_0 is the surface potential.[50] Undoubtedly, the $\chi^{(3)}$ effect is important for dilute systems with large surface charges, as the third term of eq 5 becomes significant. As discussed in the Supporting Information (Figure S7), $\left| \frac{\kappa}{\sqrt{\kappa^2 + \Delta k_z^2}} \Phi_0 \right|^2$ is about an order of magnitude smaller than the measured SFG intensities, which roughly implies that the collected data can be described using the $\chi^{(2)}$ contribution. We note that this calculation assumes a simplistic Debye length and surface charge decay, which are likely not valid for trivalent ions. In general, we focus our analysis on a qualitative discussion of the SFG data trends over subphase concentration and note that the red-shifted signal we observe is likely not from the $\chi^{(3)}$ effect. Explicitly determining the unique $\chi^{(2)}$ and $\chi^{(3)}$ contributions for trivalent ions requires additional analysis and measurements.

RESULTS AND DISCUSSION

La and Lu Ion Adsorption to GO and AA. To understand the impacts of ion size on adsorption, we determined the adsorbed La and Lu ion surface density for GO thin films and AA monolayers at the air/water interface using XFNTR. As mentioned in the Experimental Section, GO thin films were prepared at the air/water interface using a simple sonication and spreading method, investigated in detail in another work.[24] In brief, the film quality was assessed using liquid surface XR and SFG, and the prepared films are homogeneous and smooth, meaning interfacial measurements were reproducible. XFNTR is an inherently interfacial technique that measures fluorescence signals from ions within the first ~5 nm of the air/liquid surface.[45] It is element-specific and can detect[3] approximately 1 ion/50,000 $Å^2$, meaning it is well suited to quantitatively determine the number of ions adsorbed to a surfactant.

Lu^{3+} is smaller than La^{3+} and has a higher charge density per unit volume and more surface activity, as demonstrated in

https://doi.org/10.1021/acs.jpcc.3c01350
J. Phys. Chem. C 2023, 127, 14363−14373

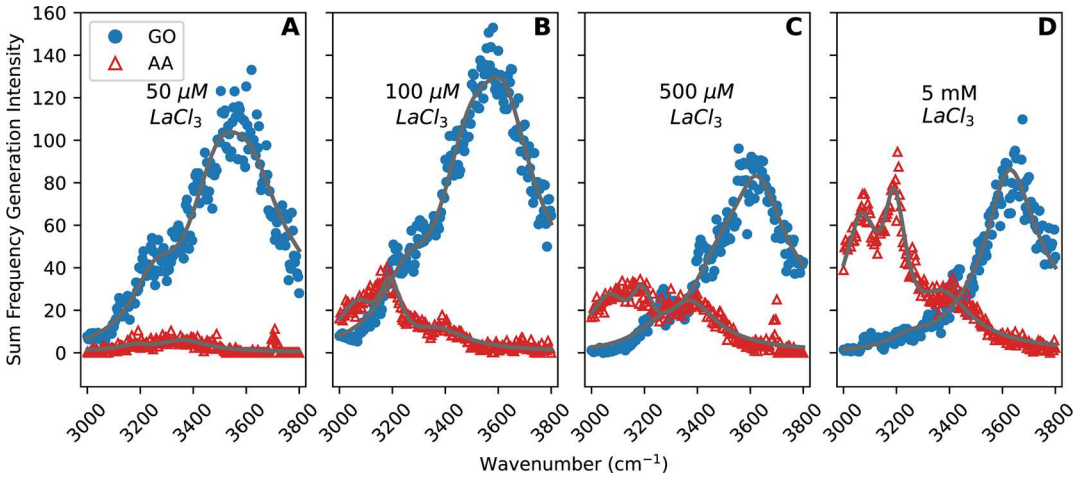

Figure 3. Normalized SFG spectroscopy intensities and fits (solid lines) of the vibrational water region plotted over wavenumber for GO thin films (blue circles) and AA monolayers (red triangles) on $LaCl_3$ subphases with different concentrations (panels). Data are normalized to a reference quartz sample and fitted to eq 4 using three Lorentzian peaks. AA monolayers were compressed to 10 mN/m, and GO thin films were compressed to 20 mN/m.

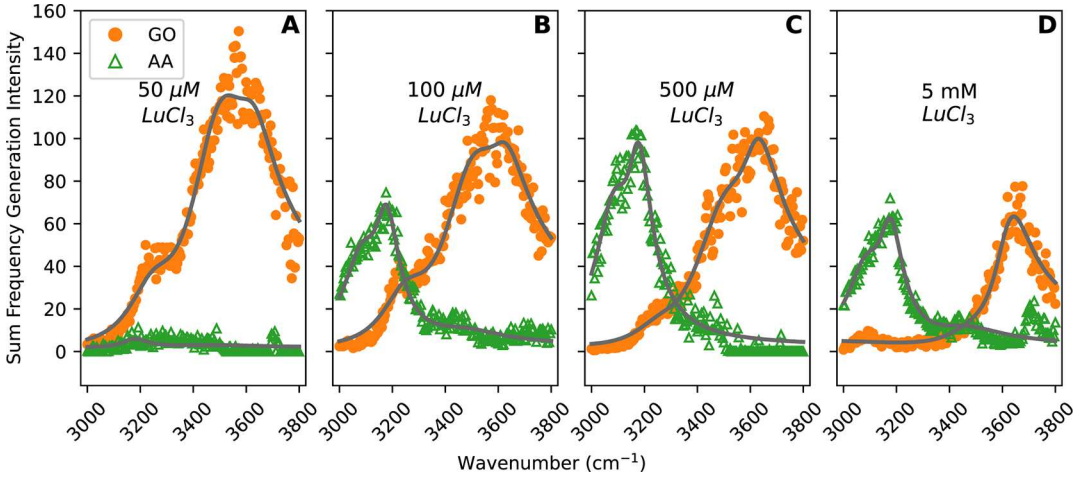

Figure 4. Normalized SFG spectroscopy intensities and fits (solid lines) of the vibrational water region plotted over wavenumber for GO thin films (orange circles) and AA monolayers (green triangles) on $LuCl_3$ subphases with different concentrations (panels). Data are normalized to a reference quartz sample and fitted to eq 4 using three Lorentzian peaks. AA monolayers were compressed to 10 mN/m, and GO thin films were compressed to 20 mN/m.

other works on rare earth adsorption.[1,3,29,44] XFNTR data (Supporting Information) for GO thin films on $LaCl_3$ and $LuCl_3$ subphases were collected for concentrations ranging from 10 μM to 20 mM, and XFNTR data for AA monolayers were collected for concentrations up to 5 mM, as AA is not a stable monolayer at higher concentrations and will collapse into micelles. For all other measured concentrations, AA exists as a monolayer, as determined by measured surface pressure/area isotherms (Supporting Information).

From these data, the adsorbed La and Lu surface densities are determined (Experimental Section) and plotted over subphase concentration to create concentration-dependent isotherms, which generally follow a Langmuir adsorption curve with one binding event for La (eq 2) and a Langmuir adsorption curve with two binding events for Lu (Figure 3). These curves are included as guides to the eye, as explicitly fitting concentration isotherm data requires additional very dilute measurements. Error bars for these surface densities are derived from the XFNTR fit. For each measured sample, the subphase pH was ~6, meaning 99% of the carboxylic acid groups of AA and GO were deprotonated, as the pK_a of AA[51] and GO[29] is 4. In this pH range, both lanthanum[52] and lutetium[29] are largely trivalent. Given that the deprotonated carboxylic acid headgroup of AA has a charge of −1, three AA molecules are required per adsorbed ion for charge compensation, which gives a surface charge density of 0.015 ions/Å^2, assuming that each AA molecule occupies 22 Å^2 at a compressed pressure of 10 mN/m (Figure 4, black horizontal line).

Reasonably, the AA monolayers achieve charge compensation with adsorbed La ions on the 50 μM subphase[1] and retain that adsorbed ion surface density as the subphase concentration increases. GO shows a similar trend but does not adsorb as many La ions after reaching maximum adsorption coverage, which is consistent with GO having fewer carboxylic acid groups per accessible thin film area as compared to AA, although GO has a more complicated interfacial structure.[24,25,28,29] For La adsorption, both surfactants qualitatively match a Langmuir adsorption isotherm with one binding event

https://doi.org/10.1021/acs.jpcc.3c01350
J. Phys. Chem. C 2023, 127, 14363−14373

despite being a simple model that does not consider specific ion-adsorption interactions or cooperative effects.

Interestingly, Lu adsorption onto GO thin films and AA monolayers is quite different (Figure 2). The AA monolayers already achieve charge compensation at the dilute subphase concentrations of 10, 50, and 100 μM $LuCl_3$, meaning the primary binding event occurs at concentrations lower than the 10 μM measured in this paper. The adsorbed Lu surface density surpasses the expected charge compensation value and continues to increase for AA monolayers measured on 500 μM and 5 mM $LuCl_3$ subphases. This additional increase in adsorbed Lu density is qualitatively indicative of a second, unique binding event. Evidently, the AA monolayers show apparent overcharging at high $LuCl_3$ concentrations, which is likely enabled by enhanced ion−ion correlations for Lu^{3+} due to its ion size compared to La^{3+}. These correlations allow Lu^{3+} ions to overcome the electrostatic repulsion between cations, meaning more Lu^{3+} can adsorb in the same area. It is also possible that hydroxide species with lower overall charge lead to increased Lu adsorption but their identification requires further investigations. Again, we note the utilized Langmuir adsorption model is simple and does not consider these more complex interactions between adsorbed ions. The trend of the experimental data is captured by considering a second, unique binding event. GO shows similar apparent overcharging for subphase concentrations greater than 5 mM. Both surfactants show preferential heavy lanthanide Lu^{3+} adsorption compared to light lanthanide La^{3+}.

When comparing Lu adsorption to AA and GO, it is important to note that GO has a more complicated layered structure at the interface, which will be examined and discussed later using XR. The preferential heavy lanthanide adsorption also demonstrates that the prepared GO films remain at the air/water interface despite the solubility of GO in the aqueous subphase. Recently, Sun et al. observed preferential light lanthanide adsorption to a fatty acid with a phosphate headgroup when the fatty acid was able to dissolve in the subphase, as heavier lanthanides in the subphase could interact with the dissolved fatty acid, thus allowing lighter lanthanides to adsorb to the surface.[3] We observe the opposite trend in our experiments where heavy lanthanide Lu preferentially adsorbs, meaning the prepared GO films remained at the interface and are available for heavy lanthanide complexation. Overall, XFNTR is a reliable and sensitive probe for determining overcharging because it quantitatively measures the amount of adsorbed metal ions within the interfacial region directly.[3,39,41,45,49]

La^{3+} and Lu^{3+} Hydration Structure during Adsorption to GO and AA. To further understand both La and Lu adsorption to GO and AA, we utilize SFG, an inherently interfacial non-linear spectroscopy technique, to probe the vibrational modes of water.[53] Normalized SFG data collected for GO thin films and AA monolayers on $LaCl_3$ subphases show a dramatic change in SFG intensity as the subphase concentration is increased (Figure 3). Data were fitted to eq 4, as described in the Experimental Section. The SFG intensity for an AA monolayer on a 50 μM $LaCl_3$ subphase shows a low signal, indicating minimal water alignment.[54] This is consistent with the previously presented XFNTR data that show La ion adsorption to the monolayer, as adsorbed metal ions disrupt the hydrogen bonding network of the interfacial water and subsequently decrease the measured SFG signal.[26,44,49] When the subphase concentration is increased to 100 μM $LaCl_3$, a new SFG peak with significant intensity emerges around 3100 cm^{-1}. This peak intensity grows for the higher-concentration 500 μM and 5 mM $LaCl_3$ subphases. As previously discussed, the XFNTR results show that the amount of adsorbed La is nearly constant in this concentration range and is consistent with the ion adsorption values expected for charge compensation, i.e., one adsorbed La^{3+} per three AA molecules (Figure 2). Together, these data suggest that this SFG peak at 3100 cm^{-1} is not indicative of ion overcharging, as interpreted previously by Sthoer et al.[52] using Y. It is important to clarify that Y has a charge density per unit volume that is more like heavy lanthanides, such as Lu, than light lanthanides. Using XFNTR, we observe apparent overcharging for heavy lanthanide adsorption to AA, meaning it is possible that Y adsorption to AA observed by Sthoer et al.[52] using SFG showed apparent overcharging as well. However, the quantitative XFNTR data on La adsorption to AA demonstrates that the emergence of the SFG signal at 3100 cm^{-1} also occurs for systems that are not overcharging, meaning this red-shifted signal is not a reliable feature of overcharged surfactants. It is also unlikely that this red-shifted signal is generated by the $\chi^{(3)}$ effect observed in collected SFG intensities for charged surfaces. Additional discussion about the $\chi^{(3)}$ contribution is provided in the Supporting Information.

Rather, we posit this SFG signal comes from the asymmetric hydration shell of the trivalent ions that directly coordinate to the carboxylic acid headgroup of AA during ion adsorption, consistent with the results of Nayak et al.[41] demonstrated with another light lanthanide, Nd. As was investigated by Sthoer et al. in detail, carboxylate groups can bind to trivalent ions in different ways by replacing the water molecules in the first coordination shell.[52] The SFG signal at 3100 cm^{-1} likely stems from the remaining water molecules in the first hydration shell. Indeed, Nayak et al. observed changes in the SFG intensity and peak position of the carboxylic acid headgroup for light lanthanide Nd adsorbed to AA.[41] Careful SFG analysis by Sthoer et al. revealed different binding motifs between the carboxylic acid headgroups and La including a bridging bidentate configuration, where metal ions adsorb to each oxygen of the deprotonated carboxylic acid group and metal ions may be additionally coordinated, and a chelating bidentate configuration, where one adsorbed metal ion may interact with both oxygens of the deprotonated carboxylic acid.[52] Multivalent ions are known to disrupt bulk hydration structures,[41] and water structure changes induced by trivalent lanthanides have been observed using Raman spectroscopy[55] and recently with SFG by our group.[41]

The SFG signal for GO thin films on $LaCl_3$ subphases shows qualitatively different behavior compared to AA. An intense SFG signal is present for films on 50, 100, and 500 μM $LaCl_3$ subphases, with two prominent peaks located around 3200 and 3400 cm^{-1}, which are generated by aligned, strongly hydrogen-bonded water and weakly hydrogen-bonded water, respectively, and are consistent with other works.[23−26,29] Such a large signal is possible because there is little La adsorbed to the GO thin film, as determined using XFNTR. With minimal adsorbed metal, water molecules can align thus creating a measurable SFG signal. At 5 mM $LaCl_3$, the measured SFG decreases significantly, except for a persistent peak around 3600 cm^{-1}, attributed to water trapped in between GO flakes within the thin film and thus unaffected by metal adsorption.[24,25,29] The overall decrease in SFG intensity is

https://doi.org/10.1021/acs.jpcc.3c01350
J. Phys. Chem. C 2023, 127, 14363−14373

consistent with a GO thin film saturated with adsorbed metal,[24,25] agreeing well with the previous XFNTR results. No significant dehydration signal near 3100 cm^{-1} appears, which implies that not enough partially dehydrated La ions adsorb to be detected using SFG.

The measured SFG signal for an AA monolayer on 50 μM $LuCl_3$ subphase (Figure 4) has a low intensity that is similar to that of the 50 μM $LaCl_3$ subphase (Figure 3). When the subphase concentration is increased to 100 μM $LuCl_3$, a significant peak appears around 3100 cm^{-1}, while the remainder of the SFG signal remains low. Similar to the SFG results on the AA monolayer on a $LaCl_3$ subphase discussed before, we attribute this signal to the partial dehydration of Lu ions that occurs during ion adsorption. Noting that the plotted SFG intensities are normalized, the absolute SFG intensity for an AA monolayer on 100 μM $LuCl_3$ is slightly larger than the SFG intensity for an AA monolayer on 100 μM $LaCl_3$, which implies more disruption within the interfacial water structure for adsorbed Lu ions versus the adsorbed La ions. This difference in SFG peak intensity is even more pronounced when comparing AA on a 500 μM $LaCl_3$ subphase to AA on a 500 μM $LuCl_3$ subphase.

Based on the XFNTR results, there are more Lu ions adsorbed to AA compared to La ions adsorbed for the 500 μM subphase, as AA shows apparent overcharging for Lu adsorption but not for La adsorption. We speculate that this is because Lu^{3+} has a larger charge density per unit volume due to its smaller size. The La^{3+}−O distance for an ion with two layers of hydration[56] is 4.65 Å, while the Lu^{3+}−O distance[57] is 4.45 Å. Lu^{3+} ions have approximately 2−4 fewer water molecules than La^{3+} in this configuration as well.[58] Consequently, Lu^{3+} has more charge per ion volume compared to La^{3+}. This increased charge density more significantly affects local ion−ion correlations and can allow more Lu^{3+} ions to adsorb[59] compared to La^{3+} even though La^{3+} has a more favorable dehydration free energy.[60] Sthoer et al. presented a detailed SFG analysis of the carboxylic acid headgroup for La and Y adsorbed to AA and observed that nearly 60% of adsorbed La participated in a bridging bidentate configuration and about 40% of adsorbed La in a chelating bidentate configuration.[52] These binding motifs were different for Y, which behaves more similarly to a heavy lanthanide, and Sthoer et al. found about 15% of adsorbed Y forms an ion pair with the carboxylic acid, 45% of the adsorbed Y exists in a bridging bidentate, and the remaining 40% of adsorbed Y exists in a chelating bidentate configuration.[52] Notably, when the charge density of the adsorbed trivalent ion changed from La to Y, the adsorption configurations also changed. Our current XFNTR and SFG data and interpretation are consistent with these results.

Interestingly, the 3100 cm^{-1} peak intensity decreases for the AA monolayer on the high-concentration 5 mM $LuCl_3$ subphase. The XFNTR data show significant apparent overcharging for AA at this subphase concentration (Figure 2), meaning the 3100 cm^{-1} peak intensity decreases when the monolayer overcharges. This is consistent with the results of Nayak et al. who observed apparent overcharging on AA monolayers when using a light lanthanide and an additional background salt via XFNTR.[41] Additionally, we note that a small signal near 3700 cm^{-1} appears inconsistently for AA spread on $LaCl_3$ (Figure 3) and $LuCl_3$ (Figure 4) subphases. Given the high frequency of this signal, it is almost certainly from dangling OH bonds that stick up out of the water surface. We suspect that it stems from water molecules that are interacting with the AA monolayer.[61] In another work, our group observed significant changes in the entire water region for a GO film on a very dilute $LuCl_3$ at pH 9, which was attributed to insoluble $Lu(OH)_3$ formation on the GO films based on SFG, XFNTR, XR, and GO membrane analysis.[29] While some partially hydrolyzed lanthanide ions exist in solution and can also affect the measured SFG intensities, we argue that it is unlikely for these species to create the signal observed at 3700 cm^{-1}.

The measured SFG data for GO thin films on $LuCl_3$ subphases (Figure 4) show large, bimodal signals for the 50, 100, and 500 μM subphases, with a slight decrease in the absolute peak intensity for the 500 μM subphase, consistent with an increase in adsorbed metal ion density, which disrupts the local water alignment and decreases the SFG signal. The GO thin film on the 5 mM $LuCl_3$ subphase shows a peak around 3100 cm^{-1}, a signal that has not been observed before for GO thin films at the air/water interface. Consistent with the interpretation of the model AA monolayer SFG data, we attribute this peak to partially dehydrated, adsorbed metal ions. Previous works have speculated that the functional groups present on GO can facilitate ion adsorption by aiding in dehydration,[2,5] and these SFG data support these claims. The lack of this signal at the lower $LuCl_3$ subphases does not imply that the adsorbed ions are fully hydrated. Rather, it means the population of dehydrated ions is either too small or not ordered enough to be detected using SFG.

GO and AA Apparent Overcharging during Lu Ion Adsorption. Collectively, the XFNTR and SFG data for both GO thin films and AA monolayers on $LaCl_3$ and $LuCl_3$ subphases can provide detailed information about ion adsorption and water structure at the air/water interface. The previously discussed XFNTR data (Figure 2) for AA monolayers on $LaCl_3$ subphases show about 3.5−3.3 AA molecules per adsorbed La, consistent with trivalent ion adsorption. It is worth noting that XFNTR is not sensitive to the metal hydration structure and can detect metal ions within ∼5 nm of the liquid surface.[45] Using a La^{3+}−O bond distance, determined experimentally with X-ray scattering,[56] of 4.65 Å, one would expect a geometric maximum of 3.4 AA molecules per La^{3+} if the metal ion retains both layers of its hydration shell. This geometric limit is not a favorable configuration for adsorbed ions, meaning it is likely that some of adsorbed La^{3+} detected using XFNTR have undergone partial dehydration of the outermost hydration shell, and possibly first hydration shell while adsorbing to the AA monolayer. This interpretation is consistent with the SFG results showing signals from an ordered population of partially dehydrated metal ions and carboxylic acid headgroups.

Similar calculations for AA monolayers on $LuCl_3$ subphases support monolayer apparent overcharging where cations continue to adsorb to the monolayer even after the system seems to achieve charge compensation. From the XFNTR data presented above (Figure 2), the calculated AA molecule per adsorbed Lu ion is ∼3.1 for a 100 μM $LuCl_3$ subphase and decreases to about 1.9 for a 5 mM $LuCl_3$ subphase, indicating significant apparent overcharging. Assuming the ions are trivalent, the geometric upper limit of Lu^{3+} ions is about 3.1 AA molecules per ion if the metal retains both layers of its hydration shell. This physical limit decreases to about 0.86 AA molecules per adsorbed Lu^{3+} if the Lu^{3+} shed the outermost hydration shell, thus decreasing the Lu^{3+}−O distance[57] to 2.34

https://doi.org/10.1021/acs.jpcc.3c01350
J. Phys. Chem. C 2023, 127, 14363−14373

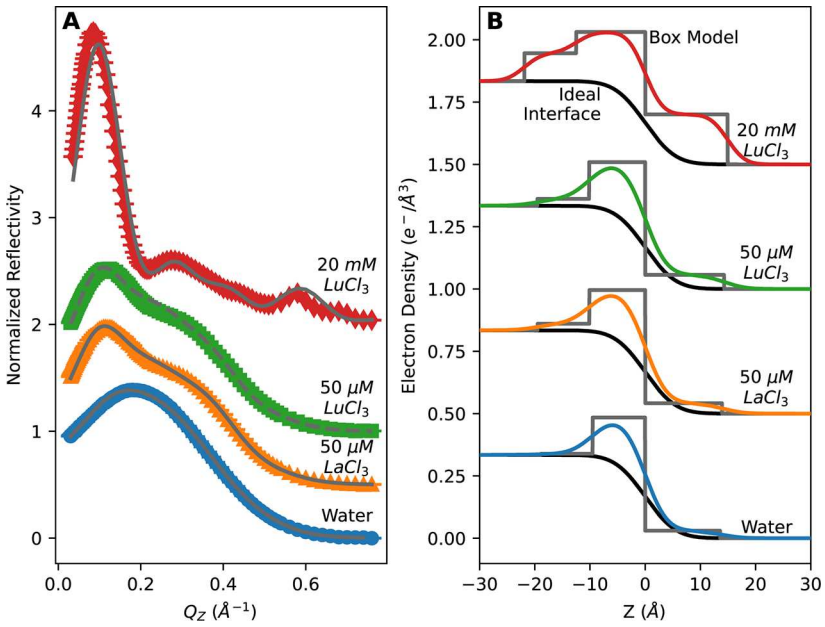

Figure 5. Normalized liquid surface XR and fits (gray lines) plotted over momentum transfer Q_Z (A) of GO thin films on different subphases (colors) and calculated electron density profiles from fitted reflectivity data (B). The corresponding box model with no roughness (gray) and an ideal interface (black) is included.

Å. Because such geometric limits are not favorable configurations, these results imply that a portion of Lu^{3+} ions partially dehydrate while adsorbing to an AA monolayer on a 100 μM $LuCl_3$ subphase. Given the amount of adsorbed Lu^{3+} ions in the 5 mM subphase case, it is not possible for all adsorbed ions to retain two full hydration shells. Instead, some Lu^{3+} ions must shed part of their water structure. These calculations agree well with the SFG results that show a red-shifted peak in the vibrational water region for AA monolayers on $LuCl_3$ subphases, which we argue is related to interfacial water reorganization from metal ion and carboxylic acid headgroup partial dehydration. Dehydration is necessary for these monolayers to accommodate the excess metal ions present during overcharging.

Interestingly, the amount of adsorbed Lu to GO is similar to that of AA for a 5 mM $LuCl_3$ subphase even though AA likely has a large surface charge because it has more carboxylic acid groups per unit area compared to GO. Another work completed by our group estimates that GO is about 8% carboxylic acid, as determined using ex situ X-ray photoelectron spectroscopy and in situ SFG.[26] However, unlike AA, GO under these experimental conditions is not a monolayer and instead has a complicated, multilayer structure at the air/water interface.[24,29] We use XR to determine the GO film structure with sub-nanometer resolution.

XR data on GO thin films on 50 μM $LaCl_3$ and $LuCl_3$ subphases are nearly identical with two features near Q_Z = 0.11 and 0.31 Å^{-1} (Figure 5). Fitting to a three-slab model gives an electron density profile consistent with previous results.[24,29] We interpret this profile as follows: one layer of GO flakes is partially submerged in the subphase, one layer sits at the air/water interface, and the last layer pushes up into the air. A GO film on plain water does not show a partially submerged layer, which implies the GO layer closest to the liquid interacts primarily with adsorbed metal ions. The electron density profiles for the films on $LaCl_3$ and $LuCl_3$ are similar because at this subphase concentration, a similar number of ions adsorb. Taken together with the XFNTR data, these data demonstrate that GO thin films show no specificity between light and heavy lanthanide ions at dilute concentrations. This implies that at low subphase concentrations, ion−ion correlations are not significant enough[48] to overcome energetically unfavorable steric hindrance between adsorbed cations. Presumably, the functional groups of GO still enable ion dehydration, but electrostatic repulsion between the cations hinders adsorption.

XR data for a GO film on a 20 mM $LuCl_3$ subphase are significantly different, with more prominent signals at Q_Z ∼0.1 and 0.3 Å^{-1} and additional features at Q_Z = 0.4 and 0.57 Å^{-1} (Figure 5). Consequently, the electron density profile shows higher density after fitting with a three-slab model. Integrating these electron density profiles gives an electron density per unit area.[29] The integrated electron density profile for a GO thin film on a 20 mM $LuCl_3$ subphase shows an excess ∼1.4 e$^-$/Å^2 after accounting for electrons from the GO thin film on plain water (i.e., electron density from the GO itself and electron density from water typically near the GO film) and electrons from the adsorbed Lu^{3+} ions. This extra electron density likely stems from additional water surrounding the adsorbed ions at the interface, which is present in much smaller amounts for films made on lower-concentration subphases, consistent with the differences in adsorbed ion densities.

Comparing the AA and GO results for $LuCl_3$ subphases allows us to demonstrate GO overcharging. An ideal monolayer of AA requires 0.015 adsorbed Lu^{3+}/Å^2 to achieve charge compensation (Figure 2). Considering that the carboxylic acid density of GO is around 8% of AA, 0.0012 Lu^{3+}/Å^2 would compensate for the surface charge of GO. XFNTR data for a GO thin film on a 20 mM $LuCl_3$ subphase has an adsorbed ion density of 0.047 ± 0.003 Lu^{3+}/Å^2, which is significantly higher than the amount needed for charge compensation of an AA monolayer. XR data for a GO film on this subphase show significantly more electron density within the two layers closest to the liquid surface, meaning adsorbed Lu^{3+} ions are not distributed evenly across the GO

https://doi.org/10.1021/acs.jpcc.3c01350
J. Phys. Chem. C 2023, 127, 14363−14373

layers. Taken together, these data suggest that GO apparently overcharges on significantly concentrated $LuCl_3$ subphases. We speculate that GO thin films can accommodate more adsorbed Lu ions than necessary for charge compensation because of their layered structure. It is possible the GO flakes can rearrange to minimize the electrostatic repulsion between adsorbed cations, which is also reduced by the subphase concentration. It is also possible that the GO itself can chemically rearrange to accommodate adsorbed Lu ions. David and Kumar show via Born−Oppenheimer molecular dynamics that GO flakes can react with pure water and form different functional groups, depending on the GO degree of oxidation.[62] It follows that GO flakes can also move protons in response to adsorbed cations. AA monolayers do not have such flexibility and therefore cannot accommodate more adsorbed ions even with improved ion−ion correlations.

CONCLUSIONS

Isolating targeted lanthanide ions from mixtures is imperative for many high-technology applications but challenging, as the metal ion extraction efficiency varies across the lanthanide series. Previous works have attributed these variations with the change in metal ion size from the lightest lanthanide La to the heaviest lanthanide Lu. In this work, we investigate the effects of lanthanide size on ion adsorption to GO thin films and AA monolayers at the air/water interface using La and Lu. Interface-specific XFNTR provides quantitative adsorbed ion densities and shows that Lu exhibits apparent overcharging when adsorbed to AA and GO on higher-concentration subphases. La adsorption is consistent with the expected charge compensation, one trivalent metal ion per three deprotonated carboxylic acid headgroups. Understanding the surface charge of GO is difficult, as GO forms a multilayer thin film at the air/water interface. XR data show three primary layers within the GO thin film with most of the electron density existing in the layers closest to the liquid surface. When combined with the adsorbed ion densities obtained by XFNTR, this data supports GO overcharges.

Additional SFG data reveal the hydration structure of the adsorbed ions to both AA and GO. The emergence of a red-shifted signal in the vibrational water region for AA is attributed to the partial metal ion and carboxylic acid headgroup dehydration during ion adsorption. Both light La and heavy Lu show this peak, meaning it is not related to monolayer overcharging. Rather, the peak intensity decreases slightly as more ions adsorb, possibly because these extra adsorbed ions disrupt local water alignment and SFG detection. This dehydration peak is also present for a GO thin film on a high-concentration subphase, which supports the argument that GO functional groups enable significant ion adsorption by facilitating ion dehydration. Taken together, these results underscore the importance of considering model monolayers in comparison to more complicated, but technologically relevant, GO thin films and highlight the necessity of multiple surface probes to detail the interface.

ASSOCIATED CONTENT

Supporting Information

The Supporting Information is available free of charge at https://pubs.acs.org/doi/10.1021/acs.jpcc.3c01350.

Pressure−area isotherms for AA monolayers, parameters for fitted XR data, and XFNTR intensity data for GO and AA (PDF)

AUTHOR INFORMATION

Corresponding Author

Ahmet Uysal − *Chemical Sciences and Engineering Division, Argonne National Laboratory, Lemont, Illinois 60439, United States;* orcid.org/0000-0003-3278-5570; Phone: +1-630-252-9133; Email: ahmet@anl.gov

Authors

Amanda J. Carr − *Chemical Sciences and Engineering Division, Argonne National Laboratory, Lemont, Illinois 60439, United States;* orcid.org/0000-0002-8224-7677

Seung Eun Lee − *Chemical Sciences and Engineering Division, Argonne National Laboratory, Lemont, Illinois 60439, United States;* orcid.org/0000-0002-5897-7266

Complete contact information is available at: https://pubs.acs.org/10.1021/acs.jpcc.3c01350

Author Contributions

The manuscript was written through contributions of all authors. All authors have given approval to the final version of the manuscript.

Notes

The authors declare no competing financial interest.

ACKNOWLEDGMENTS

We thank Wei Bu for his help with the synchrotron experiments. This material is based upon work supported by the U.S. Department of Energy, Office of Basic Energy Science, Division of Chemical Sciences, Geosciences, and Biosciences, Separation Science, Early Career Research Program under contract DE-AC02-06CH11357. Use of the Advanced Photon Source and Center for Nanoscale Materials, both Office of Science User Facilities operated for the U.S. Department of Energy (DOE) and Office of Science by Argonne National Laboratory, was supported by the U.S. DOE under contract no. DE-AC02-06CH11357. The NSF's ChemMatCARS Sector 15 is supported by the Divisions of Chemistry (CHE) and Materials Research (DMR), National Science Foundation, under grant NSF/CHE-1834750.

REFERENCES

(1) Miller, M.; Liang, Y.; Li, H.; Chu, M.; Yoo, S.; Bu, W.; Olvera de la Cruz, M.; Dutta, P. Electrostatic Origin of Element Selectivity during Rare Earth Adsorption. *Phys. Rev. Lett.* **2019**, *122*, 058001.

(2) Xie, F.; Zhang, T. A.; Dreisinger, D.; Doyle, F. A critical review on solvent extraction of rare earths from aqueous solutions. *Miner. Eng.* **2014**, *56*, 10−28.

(3) Sun, P.; Binter, E. A.; Liang, Z.; Brown, M. A.; Gelis, A. V.; Benjamin, I.; Bera, M. K.; Lin, B.; Bu, W.; Schlossman, M. L. Antagonistic Role of Aqueous Complexation in the Solvent Extraction and Separation of Rare Earth Ions. *ACS Cent. Sci.* **2021**, *7*, 1908−1918.

(4) Martinez-Gomez, N. C.; Vu, H. N.; Skovran, E. Lanthanide Chemistry: From Coordination in Chemical Complexes Shaping Our Technology to Coordination in Enzymes Shaping Bacterial Metabolism. *Inorg. Chem.* **2016**, *55*, 10083−10089.

(5) Liu, G.; Jin, W.; Xu, N. Graphene-based membranes. *Chem. Soc. Rev.* **2015**, *44*, 5016−5030.

(6) Lerf, A.; He, H.; Forster, M.; Klinowski, J. Structure of Graphite Oxide Revisited. *J. Phys. Chem. B* **1998**, *102*, 4477−4482.

(7) Hidalgo, R. S.; Lopez-Diaz, D.; Velazquez, M. M. Graphene oxide thin films: influence of chemical structure and deposition methodology. *Langmuir* **2015**, *31*, 2697−2705.
(8) Chen, J.; Chi, F.; Huang, L.; Zhang, M.; Yao, B.; Li, Y.; Li, C.; Shi, G. Synthesis of graphene oxide sheets with controlled sizes from sieved graphite flakes. *Carbon* **2016**, *110*, 34−40.
(9) Krishnamoorthy, K.; Veerapandian, M.; Yun, K.; Kim, S. J. The chemical and structural analysis of graphene oxide with different degrees of oxidation. *Carbon* **2013**, *53*, 38−49.
(10) Hu, B.; Hu, Q.; Li, X.; Pan, H.; Tang, X.; Chen, C.; Huang, C. Rapid and highly efficient removal of Eu(III) from aqueous solutions using graphene oxide. *J. Mol. Liq.* **2017**, *229*, 6−14.
(11) Xie, Y.; Helvenston, E. M.; Shuller-Nickles, L. C.; Powell, B. A. Surface Complexation Modeling of Eu(III) and U(VI) Interactions with Graphene Oxide. *Environ. Sci. Technol.* **2016**, *50*, 1821−1827.
(12) Chang, K.; Sun, Y.; Ye, F.; Li, X.; Sheng, G.; Zhao, D.; Linghu, W.; Li, H.; Liu, J. Macroscopic and molecular study of the sorption and co-sorption of graphene oxide and Eu(III) onto layered double hydroxides. *Chem. Eng. J.* **2017**, *325*, 665−671.
(13) Peng, W.; Li, H.; Liu, Y.; Song, S. A review on heavy metal ions adsorption from water by graphene oxide and its composites. *J. Mol. Liq.* **2017**, *230*, 496−504.
(14) Boulanger, N.; Kuzenkova, A. S.; Iakunkov, A.; Romanchuk, A. Y.; Trigub, A. L.; Egorov, A. V.; Bauters, S.; Amidani, L.; Retegan, M.; Kvashnina, K. O.; et al. Enhanced Sorption of Radionuclides by Defect-Rich Graphene Oxide. *ACS Appl. Mater. Interfaces* **2020**, *12*, 45122−45135.
(15) Kuzenkova, A. S.; Romanchuk, A. Y.; Trigub, A. L.; Maslakov, K. I.; Egorov, A. V.; Amidani, L.; Kittrell, C.; Kvashnina, K. O.; Tour, J. M.; Talyzin, A. V.; et al. New insights into the mechanism of graphene oxide and radionuclide interaction. *Carbon* **2020**, *158*, 291−302.
(16) Romanchuk, A. Y.; Slesarev, A. S.; Kalmykov, S. N.; Kosynkin, D. V.; Tour, J. M. Graphene oxide for effective radionuclide removal. *Phys. Chem. Chem. Phys.* **2013**, *15*, 2321−2327.
(17) Xie, Y.; Powell, B. A. Linear Free Energy Relationship for Actinide Sorption to Graphene Oxide. *ACS Appl. Mater. Interfaces* **2018**, *10*, 32086−32092.
(18) Mohamud, H.; Ivanov, P.; Russell, B. C.; Regan, P. H.; Ward, N. I. Selective sorption of uranium from aqueous solution by graphene oxide-modified materials. *J. Radioanal. Nucl. Chem.* **2018**, *316*, 839−848.
(19) Khaliha, S.; Marforio, T. D.; Kovtun, A.; Mantovani, S.; Bianchi, A.; Luisa Navacchia, M.; Zambianchi, M.; Bocchi, L.; Boulanger, N.; Iakunkov, A.; et al. Defective graphene nanosheets for drinking water purification: Adsorption mechanism, performance, and recovery. *FlatChem* **2021**, *29*, 100283.
(20) Nguyen, M. T.; Zhang, J.; Prabhakaran, V.; Tan, S.; Baxter, E. T.; Shutthanandan, V.; Johnson, G. E.; Rousseau, R.; Glezakou, V. A. Graphene Oxide as a Pb(II) Separation Medium: Has Part of the Story Been Overlooked? *JACS Au* **2021**, *1*, 766−776.
(21) Romaniak, G.; Dybowski, K.; Jeziorna, A.; Kula, P.; Kaźmierczak, T. Synthesis and characterization of semi-permeable graphene/graphene oxide membranes for water desalination. *J. Mater. Sci.* **2020**, *55*, 9775−9786.
(22) Kaewmee, P.; Manyam, J.; Opaprakasit, P.; Truc Le, G. T.; Chanlek, N.; Sreearunothai, P. Effective removal of cesium by pristine graphene oxide: performance, characterizations and mechanisms. *RSC Adv.* **2017**, *7*, 38747−38756.
(23) Hong, Y.; He, J.; Zhang, C.; Wang, X. Probing the Structure of Water at the Interface with Graphene Oxide Using Sum Frequency Generation Vibrational Spectroscopy. *J. Phys. Chem. C* **2022**, *126*, 1471−1480.
(24) Kumal, R. R.; Carr, A. J.; Uysal, A. A Simple Method for High-Quality Ultra-Thin Graphene Oxide Films Facilitates Nanoscale Investigations of Ion and Water Adsorption. *ChemRxiv* **2022**, DOI: 10.26434/chemrxiv-2022-1csxr.
(25) Carr, A. J.; Kumal, R. R.; Bu, W.; Uysal, A. Effects of ion adsorption on graphene oxide films and interfacial water structure: A molecular-scale description. *Carbon* **2022**, *195*, 131−140.
(26) Lee, S. E.; Carr, A. J.; Kumal, R. R.; Uysal, A. Monovalent Ion-Graphene Oxide Interactions are Controlled by Carboxylic Acid Groups: Sum Frequency Generation Spectroscopy Studies. *ChemRxiv* **2023**, DOI: 10.26434/chemrxiv-2023-dj4m0-v2.
(27) López-Díaz, D.; Merchán, M. D.; Velázquez, M. M.; Maestro, A. Understanding the Role of Oxidative Debris on the Structure of Graphene Oxide Films at the Air−Water Interface: A Neutron Reflectivity Study. *ACS Appl. Mater. Interfaces* **2020**, *12*, 25453−25463.
(28) Bonatout, N.; Muller, F.; Fontaine, P.; Gascon, I.; Konovalov, O.; Goldmann, M. How exfoliated graphene oxide nanosheets organize at the water interface: evidence for a spontaneous bilayer self-assembly. *Nanoscale* **2017**, *9*, 12543−12548.
(29) Carr, A. J.; Lee, S. E.; Kumal, R. R.; Bu, W.; Uysal, A. Convenient Confinement: Interplay of Solution Conditions and Graphene Oxide Film Structure on Rare Earth Separations. *ACS Appl. Mater. Interfaces* **2022**, *14*, 57133−57143.
(30) Johnson, K. R.; Driscoll, D. M.; Damron, J. T.; Ivanov, A. S.; Jansone-Popova, S. Size Selective Ligand Tug of War Strategy to Separate Rare Earth Elements. *JACS Au* **2023**, *3*, 584−591.
(31) Ellis, R. J.; Brigham, D. M.; Delmau, L.; Ivanov, A. S.; Williams, N. J.; Vo, M. N.; Reinhart, B.; Moyer, B. A.; Bryantsev, V. S. Straining to Separate the Rare Earths: How the Lanthanide Contraction Impacts Chelation by Diglycolamide Ligands. *Inorg. Chem.* **2017**, *56*, 1152−1160.
(32) Li, Z.; Binnemans, K. Hydration counteracts the separation of lanthanides by solvent extraction. *AlChE J.* **2020**, *66*, No. e16545.
(33) Ferru, G.; Reinhart, B.; Bera, M. K.; Olvera de la Cruz, M.; Qiao, B.; Ellis, R. J. The Lanthanide Contraction beyond Coordination Chemistry. *Chem.—Eur. J.* **2016**, *22*, 6899−6904.
(34) Duvail, M.; Spezia, R.; Vitorge, P. A dynamic model to explain hydration behaviour along the lanthanide series. *ChemPhysChem* **2008**, *9*, 693−696.
(35) Qiao, B.; Skanthakumar, S.; Soderholm, L. Comparative CHARMM and AMOEBA Simulations of Lanthanide Hydration Energetics and Experimental Aqueous-Solution Structures. *J. Chem. Theory Comput.* **2018**, *14*, 1781−1790.
(36) Allen, P. G.; Bucher, J. J.; Shuh, D. K.; Edelstein, N. M.; Craig, I. Coordination chemistry of trivalent lanthanide and actinide ions in dilute and concentrated chloride solutions. *Inorg. Chem.* **2000**, *39*, 595−601.
(37) Rizkalla, E. N.; Choppin, G. R. Hydration of lanthanides and actinides in solution. *J. Alloys Compd.* **1992**, *180*, 325−336.
(38) Miller, M.; Chu, M.; Lin, B.; Bu, W.; Dutta, P. Atomic Number Dependent "Structural Transitions" in Ordered Lanthanide Monolayers: Role of the Hydration Shell. *Langmuir* **2017**, *33*, 1412−1418.
(39) Nayak, S.; Kumal, R. R.; Liu, Z.; Qiao, B.; Clark, A. E.; Uysal, A. Origins of Clustering of Metalate-Extractant Complexes in Liquid-Liquid Extraction. *ACS Appl. Mater. Interfaces* **2021**, *13*, 24194−24206.
(40) Rock, W.; Qiao, B.; Zhou, T.; Clark, A. E.; Uysal, A. Heavy Anionic Complex Creates a Unique Water Structure at a Soft Charged Interface. *J. Phys. Chem. C* **2018**, *122*, 29228−29236.
(41) Nayak, S.; Kumal, R. R.; Lee, S. E.; Uysal, A. Elucidating Trivalent Ion Adsorption at Floating Carboxylic Acid Monolayers: Charge Reversal or Water Reorganization? *J. Phys. Chem. Lett.* **2023**, *14*, 3685−3690.
(42) Kumal, R. R.; Wimalasiri, P. N.; Servis, M. J.; Uysal, A. Thiocyanate Ions Form Antiparallel Populations at the Concentrated Electrolyte/Charged Surfactant Interface. *J. Phys. Chem. Lett.* **2022**, *13*, 5081−5087.
(43) Lovering, K.; Nayak, S.; Bu, W.; Uysal, A. The Role of Specific Ion Effects in Ion Transport: The Case of Nitrate and Thiocyanate. *J. Phys. Chem. C* **2019**, *124*, 573−581.

(44) Nayak, S.; Kumal, R. R.; Uysal, A. Spontaneous and Ion-Specific Formation of Inverted Bilayers at Air/Aqueous Interface. *Langmuir* **2022**, *38*, 5617−5625.
(45) Bera, M. K.; Bu, W.; Uysal, A. Liquid surface x-ray scattering. In *Physical Chemistry of Gas-Liquid Interfaces*; Faust, J., House, J., Eds.; Elsevier, 2018; pp 167−194.
(46) Danauskas, S. M.; Li, D. X.; Meron, M.; Lin, B. H.; Lee, K. Y. C. Stochastic fitting of specular X-ray reflectivity data using StochFit. *J. Appl. Crystallogr.* **2008**, *41*, 1187−1193.
(47) Schmidt, M.; Lee, S. S.; Wilson, R. E.; Soderholm, L.; Fenter, P. Sorption of tetravalent thorium on muscovite. *Geochim. Cosmochim. Acta* **2012**, *88*, 66−76.
(48) Lee, S. S.; Koishi, A.; Bourg, I. C.; Fenter, P. Ion correlations drive charge overscreening and heterogeneous nucleation at solid-aqueous electrolyte interfaces. *Proc. Natl. Acad. Sci. U.S.A.* **2021**, *118*, 118.
(49) Kumal, R. R.; Nayak, S.; Bu, W.; Uysal, A. Chemical Potential Driven Reorganization of Anions between Stern and Diffuse Layers at the Air/Water Interface. *J. Phys. Chem. C* **2022**, *126*, 1140−1151.
(50) Ohno, P. E.; Wang, H. F.; Geiger, F. M. Second-order spectral lineshapes from charged interfaces. *Nat. Commun.* **2017**, *8*, 1032.
(51) Vysotsky, Y. B.; Kartashynska, E. S.; Vollhardt, D.; Fainerman, V. B. Surface pKa of Saturated Carboxylic Acids at the Air/Water Interface: A Quantum Chemical Approach. *J. Phys. Chem. C* **2020**, *124*, 13809−13818.
(52) Sthoer, A.; Adams, E. M.; Sengupta, S.; Corkery, R. W.; Allen, H. C.; Tyrode, E. C. La3+ and Y3+ interactions with the carboxylic acid moiety at the liquid/vapor interface: Identification of binding complexes, charge reversal, and detection limits. *J. Colloid Interface Sci.* **2022**, *608*, 2169−2180.
(53) Johnson, C. M.; Baldelli, S. Vibrational Sum Frequency Spectroscopy Studies of the Influence of Solutes and Phospholipids at Vapor/Water Interfaces Relevant to Biological and Environmental Systems. *Chem. Rev.* **2014**, *114*, 8416−8446.
(54) Geiger, F. M. Second Harmonic Generation, Sum Frequency Generation, and $\chi^{(3)}$: Dissecting Environmental Interfaces with a Nonlinear Optical Swiss Army Knife. *Annu. Rev. Phys. Chem.* **2009**, *60*, 61−83.
(55) Patra, A.; Roy, S.; Saha, S.; Palit, D. K.; Mondal, J. A. Observation of Extremely Weakly Interacting OH (~3600 cm^{-1}) in the Vicinity of High Charge Density Metal Ions (M^{z+}; z = 1, 2, 3): A Structural Heterogeneity in the Extended Hydration Shell. *J. Phys. Chem. C* **2020**, *124*, 3028−3036.
(56) Habenschuss, A.; Spedding, F. H. The coordination (hydration) of rare earth ions in aqueous chloride solutions from X-ray diffraction. II. (LaCl3, PrCl3, and NdCl3a). *J. Chem. Phys.* **1979**, *70*, 3758−3763.
(57) Habenschuss, A.; Spedding, F. H. The coordination (hydration) of rare earth ions in aqueous chloride solutions from X-ray diffraction. I. TbCl3, DyCl3, ErCl3, TmCl3, and LuCl3. *J. Chem. Phys.* **1979**, *70*, 2797−2806.
(58) Smirnov, P. R.; Trostin, V. N. Structural parameters of close surroundings of Sr2+ and Ba2+ ions in aqueous solutions of their salts. *Russ. J. Gen. Chem.* **2011**, *81*, 282−289.
(59) Miller, M.; Chu, M.; Lin, B.; Meron, M.; Dutta, P. Observation of Ordered Structures in Counterion Layers near Wet Charged Surfaces: A Potential Mechanism for Charge Inversion. *Langmuir* **2016**, *32*, 73−77.
(60) Marcus, Y. A simple empirical model describing the thermodynamics of hydration of ions of widely varying charges, sizes, and shapes. *Biophys. Chem.* **1994**, *51*, 111−127.
(61) Sartin, M. M.; Sung, W.; Nihonyanagi, S.; Tahara, T. Molecular mechanism of charge inversion revealed by polar orientation of interfacial water molecules: A heterodyne-detected vibrational sum frequency generation study. *J. Chem. Phys.* **2018**, *149*, 024703.
(62) David, R.; Kumar, R. Reactive events at the graphene oxide-water interface. *Chem. Commun.* **2021**, *57*, 11697−11700.

https://doi.org/10.1021/acs.jpcc.3c01350
J. Phys. Chem. C 2023, 127, 14363−14373